A Review of Actuation and Power Electronics Options for Flapping-Wing Robotic Insects

Michael Karpelson, Gu-Yeon Wei, *Member, IEEE,* Robert J. Wood, *Member, IEEE*

Abstract— Flapping-wing robotic insects require actuators with high power densities at centimeter to micrometer scales. Due to the low weight budget, the selection and design of the actuation mechanism needs to be considered in parallel with the design of the power electronics required to drive it. This paper explores the design space of flapping-wing microrobots weighing 1g and under by determining mechanical requirements for the actuation mechanism, analyzing potential actuation technologies, and discussing the design and realization of the required power electronics. Promising combinations of actuators and power circuits are identified and used to estimate microrobot performance.

Index Terms— microrobots, MAV, actuator, power electronics

I. INTRODUCTION

Flapping-wing micro air vehicles (MAVs) are centimeter-scale flying robots with potential applications in search-and-rescue, exploration, and reconnaissance. These robotic platforms frequently take design cues from flying insects in an attempt to achieve a similar maneuverability, efficiency, and hovering ability. Several prototypes of insect-sized flapping-wing MAVs have shown promise, including the Micromechanical Flying Insect [1] and the Harvard Microrobotic Fly [2].

One of the main challenges in MAV design is the selection of an actuation scheme that can provide sufficient power for autonomous flight. When the characteristic dimension of the robot falls below 1mm, conventional actuators, such as electromagnetic motors, begin to see a considerable reduction in efficiency and power density due to an increased dominance of surface effects [3]. A number of alternative methods, such as piezoelectric [1] or thermal [4] actuators, have been suggested for small-scale flying robots. In addition to varying mechanical capabilities, these actuation techniques have diverse electrical requirements, including wide variations in driving voltages and currents. It is therefore necessary to consider MAV actuator selection and power electronics design as a single problem.

This paper explores the design space of flapping-wing MAVs weighing 1g and under – consisting of the aerodynamic and mechanical components, the actuator, the power electronics, and the power source of the robot – in order to identify promising combinations of actuation schemes and their associated power electronics. Actuators are evaluated in terms of the weight and power requirements of several MAV configurations, determined using an aerodynamic wing

The authors are with the School of Engineering and Applied Sciences, Harvard University, Cambridge, MA 02138, USA (contact e-mail: michaelk@seas.harvard.edu)

model. The design of the power electronics applicable to the various types of actuators is discussed, including the realization of several compact high-voltage power supplies.

II. DESIGN SPACE AND APPROACH

The subsystems of a flapping-wing MAV will be represented with the following abstractions: power source, power and drive electronics, an actuation mechanism, mechanical transmission and structural elements, and aerodynamic components. Each stage can be described in terms of mass (m), power output (P), and efficiency (η), as shown in the block diagram in Fig. 1. The goal is to select and size the components of each stage to deliver sufficient power P_{out} from the wings to permit flight.
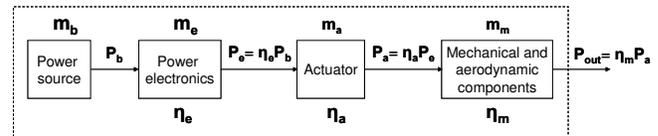

Fig. 1. Block diagram of MAV (adapted from [3]).

When the parameters listed in Fig. 1 are known, it is possible to determine the flight time of the robot using:

$$t_f = \frac{E_b \eta_e \eta_a \eta_m}{P_{out}}, \qquad (1)$$

where E_b is the energy capacity of the battery.

This paper attempts a top-down approach that uses the value of P_{out} to determine successively the requirements for the aerodynamic and mechanical components (Section III), the actuation mechanism (Section IV), and the power electronics (Section V), with the remaining mass devoted to the power source.

III. AERODYNAMIC AND MECHANICAL COMPONENTS

During hover, the actuators must provide a minimum energy at the desired flapping frequency. Actuator force and deflection are determined by the transmission mechanics, the geometry of the wings, and their flapping kinematics. For example, to support a given weight, a vehicle could flap smaller wings at high frequency, or larger wings at a lower frequency. In general, flapping slower with larger wings will, aerodynamically, be more power efficient. However, if an actuator has a higher power density at higher frequencies, then the increased power required to flap at that higher frequency could be offset by the increased energy available, due to the additional battery weight that can be carried. The

large size of the design space for the actuators, wing shapes, and kinematics puts a treatment of optimal vehicle design outside the scope of this paper.

A simple blade-element aerodynamic model can be used to determine force, deflection, and power requirements for hovering. As a quick starting point, flapping frequencies observed in insects can be used. The blade element approach used here is very similar to formulations in [1], [5], where details omitted here can be found. The wing is divided into chord-wise strips, and the force coefficients, which are a function of angle of attack, are provided by previous experiments with dynamically scaled wing models [5].

The design space of a flapping vehicle's wings is very large. Many approximations must be made to reduce the test matrix. For this model, there are two wings, which are assumed to have an aspect ratio of 4 (wing length over mean chord). They are assumed to flap in the horizontal plane, with symmetric and sinusoidal flapping and rotation kinematics. The total flapping angle is fixed at 120 degrees, and the mid-flap angle of attack is taken to be 45 degrees. In addition, the wing center of area is taken at half-span, with the second moment of area derived from Ellington's empirical relationship [6]. These design space limiting assumptions are in line with previous assumptions in similar models [7], and recently measured passive-rotation kinematics for micromechanical flying insects [2].

MAV mass and flapping frequency breakpoints were selected using insect data as a guide, and are shown in Fig. 2. For each breakpoint, the wing length was iterated over until the lift generated equaled the desired vehicle weight. The resulting wing lengths, and the power required to hover each vehicle, are shown in Table I. The profile power (viscous losses), calculated from the blade-element model, is added to the induced power (3D losses), which is estimated using the method of [7]. Any inertial power is assumed to be fully recovered from elastic storage within the actuator and thorax. Also calculated were the required driving moments (details omitted here for brevity) and actuator deflections for each design, which were used, along with frequency, as actuator requirements. The driving moments were found by integrating the differential aerodynamic moments from the blade-element model along the wing.

To ensure that an actuator will provide sufficient deflection, an assumption of the maximum possible transmission ratio must be made. For this investigation, a single-stage lever-arm was assumed, which has a transmission ratio, in radians per input displacement (for small angles) of approximately one over the length of the short link in the lever. A length of $50\mu m$ was chosen, which considers expected improvements over previous transmissions of this type [2]. For 120 degrees total flapping angle, this translates into approximately 100μm actuator peak-to-peak deflection.

For this study, the wings, transmission, and airframe are assumed to have a 20% mass fraction. This estimate is based on actual fabrication experience of robotic insects [2]. Further experimental work should help uncover scaling trends for this mass fraction.
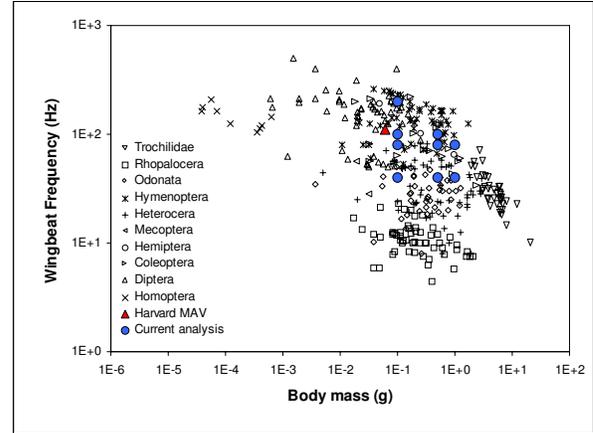

Fig. 2. Insect data from [8]. Red triangle is the Harvard 60mg MAV and the blue circles are the chosen design breakpoints.

TABLE I
MAV Configurations

Mass (g)	Flapping frequency (Hz)	Wing length (mm)	Lift (2 wings, mN)	Input power (mW)	Power density (W/kg)
0.1	40	20.75	0.98	2.76	27.64
0.1	80	14.67	0.98	3.91	39.06
0.1	100	13.12	0.98	4.36	43.64
0.1	200	9.28	0.98	6.18	61.75
0.5	40	31.03	4.90	20.67	41.34
0.5	80	21.94	4.90	29.22	58.45
0.5	100	19.62	4.90	32.64	65.29
1.0	40	36.89	9.80	49.04	49.04
1.0	80	26.09	9.80	69.49	69.49

IV. Actuator Selection

There is a number of actuation mechanisms applicable to flapping-wing MAVs. This paper focuses on relatively mature technologies that have been realized previously in the context of microrobotics. The emphasis is on linear actuators, which simplify the mechanical transmission for flapping motions. Candidate actuators have high power densities at the centimeter to micrometer scales and favorable scaling effects as actuator size is reduced. The technologies selected for analysis can be divided into five categories: electrostatic [9], piezoelectric [10], thermal [11], shape memory [12], and dielectric elastomer [13]. An overview of the categories is given in Table II.

In order to evaluate the performance of the five actuator categories, simplified models were developed for the representative actuator geometries described in Table II. The models, detailed in Table III, consist of analytical expressions for the free-end displacement, blocked force, and maximum operating frequency of the actuators based on geometric parameters, material properties, and applied excitation. These figures of merit determine whether a given actuator geometry can fulfill the mechanical requirements determined in Section III. Note that some of the actuators

TABLE II

ACTUATOR CATEGORIES

Actuator category	Operating principle	Representative geometries	Maximum deflection	Maximum force	Speed of actuation	Efficiency range (%)	Notes
Electrostatic	Electrostatic force	Comb drive, parallel plate	Low	Low	Very fast	> 90	Requires MEMS manufacturing processes, high operating voltage.
Thermal	Thermal expansion	Expansion, bimaterial bending cantilever	Medium	Very high	Slow	< 5	Versatile geometries, largest materials selection.
Piezoelectric cantilever	Converse piezoelectric effect	Bimorph, unimorph bending cantilevers	High	Medium	Fast	10-30	Simple planar structure, high operating voltage.
Shape memory alloy	Thermally induced phase change	Wire, bimaterial bending cantilever	High	Very high	Slow	< 5	Very high energy density.
Dielectric elastomer	Maxwell stress causing viscoelastic deformation	Linear extender	Highest	Medium	Medium	60-90	Capable of over 300% strain, very high operating voltage.

presented here exhibit considerable nonlinearity in their properties, making it difficult to find accurate closed-form solutions. Our analysis makes many simplifying assumptions, such as linear elastic behavior, in order to gain a general understanding of the performance and scaling characteristics of the actuators. These first-order models allow us to perform a system-level optimization to determine the appropriate actuator morphology and geometry for a target MAV.
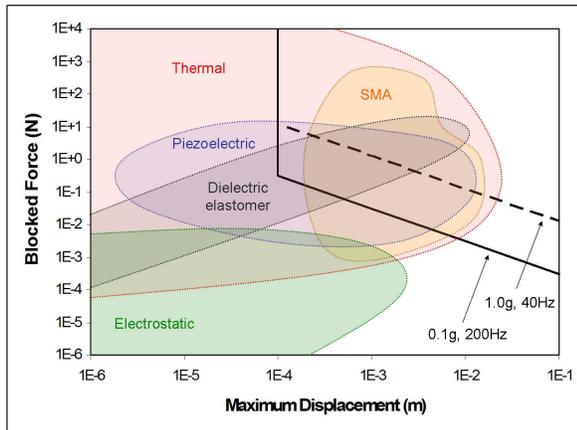

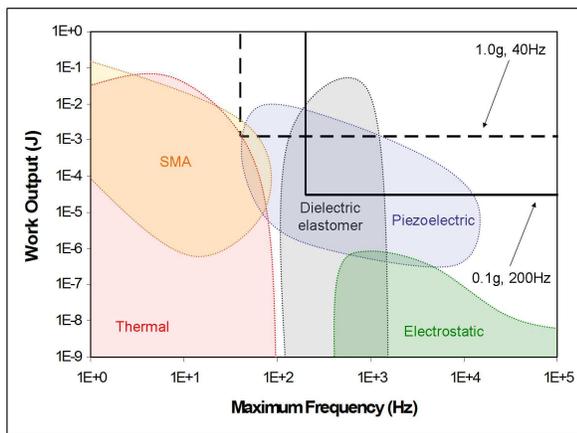Fig. 3.   Blocked force vs. maximum deflection of selected actuators.

Figures 3-5 were produced using the simplified actuator models by iterating over reasonable geometries and driving conditions. The geometric constraints and operating regimes were chosen by considering maximum MAV size, as determined by the wingspan in Section III, the physical limits of the materials involved, and the limitations of expected manufacturing processes. Fig. 3 shows the force-displacement space of the selected actuators, Fig. 4 shows the work output vs. the maximum operating frequency, and Fig. 5 shows the power density vs. the approximate actuator mass. Each graph also shows the range of requirements for the plotted quantities as determined by the MAV configurations listed in Table I.

Due to an insufficient work output, electrostatic actuators are not a viable option for MAVs in the weight categories considered in this paper. However, their high operating frequency and power density suggests potential for microgram-scale robots, as well as robots with lower energy requirements when combined with stepping or ratcheting mechanisms [17]. Thermal and shape memory alloy actuators, which meet the requirements for force and displacement, are hampered by the low operating frequencies associated with the heating and cooling of the active material (although operating frequencies scale favorably with the reduction of actuator size, due to a rapid decrease in actuator volume).
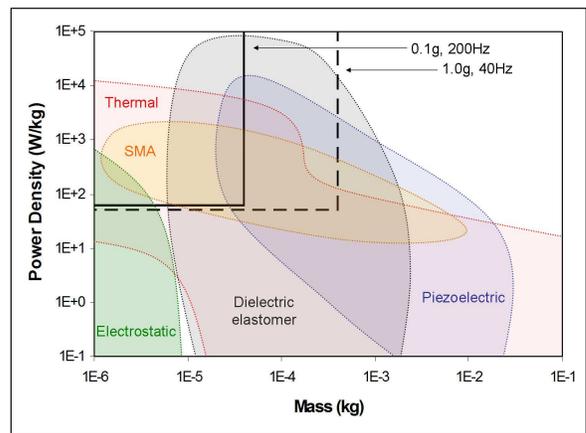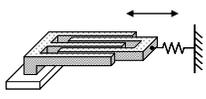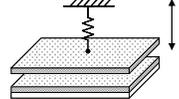

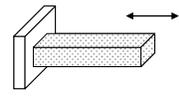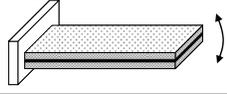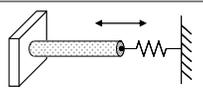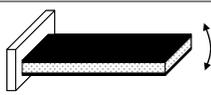Fig. 4.   Work output vs. maximum frequency of selected actuators.

Fig. 5.   Power density vs. mass of selected actuators.

TABLE III

ACTUATOR MODELS

Actuator	Comb Drive [9]	Parallel Plate [14]	Thermal Expansion [15]	Thermal Bimaterial Cantilever [11]
Geometry				
Free-end deflection	$\min\left(\frac{N\varepsilon t V^2}{2gk}, L-x\right)$	$\min\left(\frac{\varepsilon L w V^2}{2g^2 k}, \frac{g}{3}\right)$	$L\alpha(T_h - T_l)$	$\frac{3L^2(\Delta\alpha)(T_h-T_l)AB^2(B+1)}{t_1\left((AB+1)(AB^3+1)+3AB(B+1)^2\right)}$
Blocked force	$\frac{N\varepsilon t V^2}{2g}$	$\frac{\varepsilon L w V^2}{2g^2}$	$Etw\alpha(T_h - T_l)$	$\frac{E_1 t_1^2(\Delta\alpha)(T_h-T_l)(B+1)}{2B(AB+1)L}$
Maximum frequency	$\frac{1}{2\pi}\sqrt{\frac{k}{M}}$	$\frac{1}{2\pi}\sqrt{\frac{k}{M}}$	$\frac{2h(Lw+wt+Lt)}{\rho c L t w}\left[\ln\left(\frac{T_h-T_a}{T_l-T_a}\right)\right]^{-1}$	$\min\left(\frac{2h_1}{\rho_1 c_1 t_1}, \frac{2h_2}{\rho_2 c_2 t_2}\right)\left[\ln\left(\frac{T_h-T_a}{T_l-T_a}\right)\right]^{-1}$
Definitions	L - Comb finger length w - Comb finger width t - Comb thickness g - Gap between fingers N - Number of fingers x - Finger overlap	L - Length of plates w - Width of plates g - Gap between plates	L - Length (direction of expansion) w - Width t - Thickness	Subscripts 1 and 2 refer to the two materials. L - Cantilever length w - Cantilever width t - Cantilever thickness $A = E_1/E_2, B = t_1/t_2$

V - Applied voltage $\quad\quad$ E - Young's modulus $\quad\quad$ h - Convective heat transfer coefficient
ε - Permittivity of medium $\quad\quad$ ρ - Density $\quad\quad$ α - Thermal expansion coefficient
M - Mass of moving comb/plate $\quad\quad$ c - Specific heat $\quad\quad$ T_h - Maximum actuation temperature
k - Spring constant of suspension $\quad\quad$ T_a - Ambient temperature $\quad\quad$ T_l - Minimum actuation temperature

Actuator	Piezoelectric Bimorph [10]		Piezoelectric Unimorph [10]	
Geometry				
Free-end deflection	$\frac{3d_{31}L^2 V}{2(2t_p+t_s)t_p}$	$\frac{(B+1)(2B+1)}{AB^3+3B^2+3B+1}$	$\frac{3d_{31}L^2 V}{2t_p^2}$	$\frac{2AB(B+1)}{A^2B^4+2A(2B+3B^2+2B^3)+1}$
Blocked force	$\frac{3d_{31}E_p w(2t_p+t_s)^2 V}{8Lt_p}$	$\frac{2B+1}{(B+1)^2}$	$\frac{3d_{31}E_p w(t_p+t_s)^2 V}{8Lt_p}$	$\frac{2AB}{(AB+1)(B+1)}$
Maximum frequency	$\frac{3.52(2t_p+t_s)}{4\pi L^2}\sqrt{\frac{E_p}{3\rho_p}}$	$\sqrt{\frac{1+3(2B+1)^2+4AB^3}{4(B+1)^2(BC+1)}}$	$\frac{3.52(t_p+t_s)}{4\pi L^2}\sqrt{\frac{E_p}{3\rho_p}}$	$\sqrt{\frac{1+2A(2B+3B^2+2B^3)+A^2B^4}{(B+1)^2(AB+1)(BC+1)}}$
Definitions	Subscripts p and s refer to the piezoelectric layer(s) and the support layer, respectively. V - Applied voltage $\quad$ L - Cantilever length $\quad$ w - Cantilever width $\quad$ t - Thickness $\quad$ E - Young's modulus $\quad$ ρ - Density d_{31} - Transverse piezoelectric coefficient $\quad$ $A = E_s/E_p, B = t_s/2t_p$ (bimorph), $B = t_s/t_p$ (unimorph), $C = \rho_s/\rho_p$			

Actuator	SMA Wire [16]	SMA Bimaterial Cantilever [12]	Dielectric Elastomer [13]
Geometry			
Free-end deflection	$\min\left(\varepsilon_r L, \frac{E\varepsilon_r\pi r^2}{k}\right)$	$\frac{3\varepsilon_r L^2 AB^2(B+1)}{t_a\left((AB+1)(AB^3+1)+3AB(B+1)^2\right)}$	$\frac{\varepsilon L V^2}{2Et^2}$
Blocked force	$E\varepsilon_r\pi r^2$	$\frac{E_a t_a^2\varepsilon_r(B+1)}{2B(AB+1)L}$	$\frac{\varepsilon w V^2}{2t}$
Maximum frequency	$\frac{2h}{\rho cr}\left[\ln\left(\frac{T_h-T_a}{T_l-T_a}\right)\right]^{-1}$	$\frac{2h_a}{\rho_a c_a t_a}\left[\ln\left(\frac{T_h-T_a}{T_l-T_a}\right)\right]^{-1}$	$\frac{1}{2\pi}\sqrt{\frac{E}{L^2\rho}}$
Definitions	L - Length r - Radius k - Spring constant of restoring spring	Subscripts a and s refer to the SMA layer and the support layer, respectively. L - Cantilever length $\quad$ w - Cantilever width t - Thickness $\quad\quad$ $A = E_a/E_s, B = t_a/t_s$	L - Length (direction of expansion) w - Width t - Thickness E - Young's modulus

h - Convective heat transfer coefficient $\quad$ c - Specific heat $\quad$ ρ - Density $\quad\quad$ ρ - Density
E - Young's modulus $\quad\quad$ T_h - Maximum actuation temperature $\quad\quad$ ε - Permittivity of material
T_a - Ambient temperature $\quad\quad$ T_l - Minimum actuation temperature

Therefore, these actuators are best suited to (a) MAVs with lower wing flapping frequencies, and (b) MAVs that are sufficiently small as to allow the frequency scaling effect to become significant. Finally, the most suitable performance is expected from the piezoelectric and the dielectric elastomer actuator categories, which should be able to meet the actuation requirements of several MAV configurations.

Actuator efficiency is strongly dependent on the exact actuator implementation, and therefore it is difficult to model accurately, particularly for the complex heat loss processes of temperature-activated materials. Common values found in literature [12], [13], [18], listed in Table II, are used to estimate efficiency.

In order to reduce the actuator-electronics design space to manageable proportions, the maximum dimensions of an actuator intended for a given MAV are restricted by the wingspans listed in Table I. Additionally the mass of flight muscle as a percentage of body mass of biological insects is used as a guideline for the weight budget of the actuator. This quantity is in the range of 12-65%, with a midrange value of 40% selected for this analysis [19].

Based on these restrictions, specific geometries were se-

TABLE IV

APPROXIMATE ACTUATOR DIMENSIONS AND ELECTRICAL REQUIREMENTS

	Piezoelectric bimorph cantilever				SMA bending cantilever				Dielectric elastomer extender			
MAV configuration	Mass (mg)	Dimension (mm)	Voltage (V)	Current (mA)	Mass (mg)	Dimension (mm)	Voltage (V)	Current (mA)	Mass (mg)	Dimension (mm)	Voltage (V)	Current (μA)
0.1g, 40Hz	32	5.1	165	0.06	5	8.7	3.7	18.7	22	7.4	1100	3.35
0.1g, 80Hz	32	5.1	140	0.09			n/a		22	7.4	1000	5.21
0.1g, 100Hz	32	5.1	140	0.10			n/a		22	7.4	1000	5.82
0.1g, 200Hz	32	5.1	110	0.19			n/a		22	7.1	900	9.15
0.5g, 40Hz	90	9.5	190	0.36	25	23.3	3.7	140.0	57	9.0	1500	18.4
0.5g, 80Hz	62	7.8	165	0.59			n/a		57	9.2	1400	27.8
0.5g, 100Hz	60	6.4	165	0.66			n/a		62	9.0	1300	33.5
1.0g, 40Hz	207	17.8	220	0.74			n/a		64	9.0	1800	36.3
1.0g, 80Hz	154	11.7	190	1.22			n/a		58	9.0	1700	54.5

lected from the body of actuators able to meet the mechanical requirements of certain MAV configurations. Table IV lists the weights and maximum dimensions associated with these geometries, as well as the average voltage and currents required to drive them (a 3.7V single-cell lithium polymer voltage source is assumed as a starting point for thermal and SMA actuators, although other operating voltages are also possible). Electronic circuits that may be used to fulfill these requirements are discussed in the next section.

V. POWER SOURCE AND POWER ELECTRONICS

Promising microrobotic power sources include conventional chemical batteries, supercapacitors [20], fuel cells [21], and solar cells [22]. At present, conventional batteries are the only technology available commercially that is appropriate for MAV sizes discussed here. The highest power densities in such batteries are achieved by lithium polymer chemistry. Fig. 6 shows the power density and energy storage capacity vs. the battery weight for several commercially available Fullriver batteries discharged at 5C. This analysis assumes a single-cell lithium polymer battery with a capacity that scales linearly according to the trend of Fig. 6. In reality, very small batteries will see a reduced capacity due to increased packaging overhead. The projected battery storage capacity is derated according to typical battery discharge curves in cases where high discharge currents are required.

From the perspective of power and drive electronics, the actuation techniques described earlier can be separated into two categories. Thermal and shape memory actuators, which require high currents but not overly high voltages to operate, will be termed current-mode actuators. Piezoelectric, electrostatic, and dielectric elastomer actuators, which require high voltages and low currents, will be termed voltage-mode actuators. In both cases, an efficient, compact interface is required between the actuator and the battery. This interface usually consists of a power stage, which converts the battery voltage to some required level, and a driving stage, which converts the output of the power stage into a time-varying signal across the input terminals of the actuator. This section presents potential solutions to this design problem for both current-mode and voltage-mode actuators.

A. Current-mode Actuators

This category of actuators relies on high currents to raise the temperature of the active material through resistive heating. In many cases, the voltage delivered to the actuator can be lower than the battery voltage. Occasionally, a higher voltage may be used (for example, to run sufficient current through a resistive heating element without using an active current source).

One of the simplest ways to convert the battery voltage to the required level is to use the well-known buck or boost switching converters. Within a moderate voltage gain range of 0.1 to 10, which is expected to satisfy the requirements of most current-mode actuators, switching converters can achieve efficiencies of over 90%. High-frequency monolithic switching regulators are available from many semiconductor manufacturers in lightweight packaging, bringing the total weight of the converter to under 30mg (for example, using the LM2733 part from National Semiconductor with a 2.2μH inductor).

Since the operating voltage is comparatively low, the drive signal for the actuators can be generated with a wide variety of integrated linear or switching amplifiers, or simple transistor switching electronics. For the purposes of this analysis, a
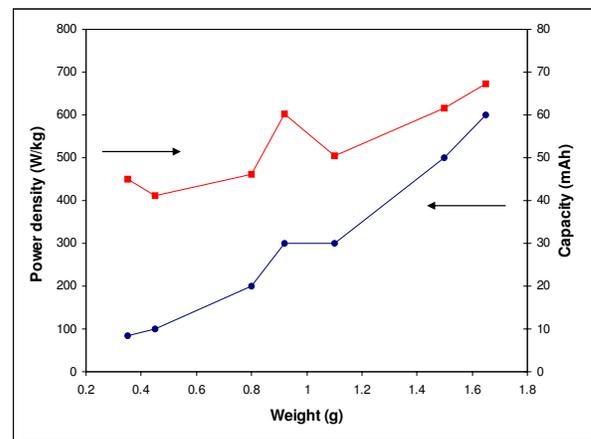

Fig. 6. Power densities and capacities of commercial Li-poly batteries discharged at 5C.
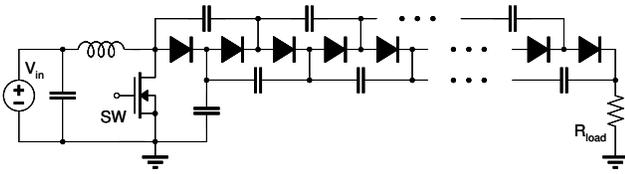
Fig. 7. Hybrid voltage multiplier.

Fig. 8. Boost converter with autotransformer.

buck or boost converter combined with a switching transistor driver is assumed, with an overall efficiency of 85%. Based on a survey of commercially available discrete components, a weight of 50mg, not including the circuit board, is estimated.

B. Voltage-mode Actuators

This category of actuators requires high voltages, from tens to thousands of volts, in order to produce sufficient electrostatic forces or high electric fields. Unlike current-mode actuators, where voltage gains are unlikely to exceed 10, voltage-mode actuators may necessitate voltage gains of up to several hundred. Due to losses in the inductor and switching transistor, as well as a very high duty cycle, the conventional boost converter becomes impractical in these cases. Three alternative techniques are presented to achieve high voltages in a compact package: a boost converter/voltage multiplier hybrid, a boost converter combined with an autotransformer, and a power amplifier using a piezoelectric transformer.

1) Hybrid Voltage Multiplier

A hybrid circuit consisting of a conventional boost converter cascaded with a switched-capacitor charge pump circuit, as shown in Fig. 7, has been considered previously for piezoelectric microrobots [3] and electrostatic MEMS devices [23]. Operating in a regime of high efficiency, the boost converter stage provides a moderate boost to the input voltage, while its pulsed output naturally charges up the capacitor ladder through the diodes. The charge pump multiplies the boost converter's output voltage, ideally by a factor equal to the number of charge pump stages. The maximum output power is limited by the size of the charge pump capacitors and the maximum output power of the boost converter.

2) Boost Converter with Autotransformer

Replacing the inductor in the standard boost converter with an autotransformer, as shown in Fig. 8, results in a combination of the boost and flyback voltage converter topologies [24]. Similar to the boost converter, current ramps up in the primary winding of the transformer when the switching transistor is conducting. When the switch turns off, the rectifier diode sees a combination of the input voltage, the primary winding voltage, and the secondary winding voltage, which depends on the turns ratio between the primary and secondary windings. Voltage gain is therefore determined by the duty cycle of the switching transistor and the turn ratio of the transformer. Maximum output power is limited by the current rating of the switching transistor and the transformer.
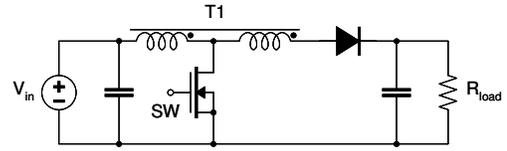
For high voltage gains, this method has a much lower parts count than the hybrid converter. However, the rectifier diode and output capacitor must be rated for the output voltage. Additionally, a custom transformer may be required, since no commercial parts under 2g could be identified.

3) Piezoelectric Power Amplifier

Piezoelectric transformers (PTs) have a high voltage gain ratio and high power density (up to 40W/cm^3) [25]. Due to their simple geometries, they scale better to small sizes than magnetic transformers and hold potential for on-chip integration. Many geometries exist with the same basic operating principle - the "primary" side of the PT excites mechanical oscillations in the piezoelectric material, while the "secondary" side generates a voltage. PT geometries suitable for step-up applications are described in [25].

In order to obtain high voltage gain and efficiency, a PT has to operate close to the mechanical resonance frequency, where its electrical response can be approximated by the equivalent circuit in Fig. 9(a). The gain of a PT is also highest at low loads, making it a good candidate for the high-voltage, low-current requirements of voltage-mode actuators. In order to reduce switching losses, as well as losses associated with charging and discharging the input capacitance of the PT, a resonant driving stage is used [26].

Fig. 9(b) shows the Class "E" resonant topology, selected here because it has a low number of additional components. The inductor is selected to resonate with the input capacitance C_{in} of the PT at a frequency close to the mechanical resonance frequency. The resonance transfers energy to the PT from the inductor when the switch is off. The switch is turned on again as soon as the voltage across C_{in} rings
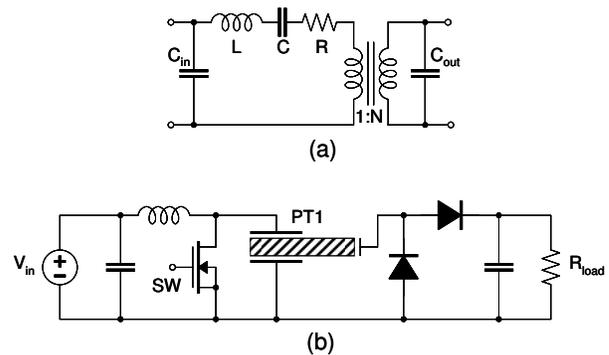

(a)

(b)

Fig. 9. Piezoelectric transformer equivalent circuit (a) and Class "E" power amplifier (b).

TABLE V

VOLTAGE CONVERTER CONFIGURATIONS

	High-power hybrid	Low-power hybrid	Autotransformer
Component weight	150mg	80mg	80mg
Board area (two sides)	1.5cm^2	1.2cm^2	0.5cm^2
Regulator	Linear LT1615 (PFM)	Linear LT1615-1 (PFM)	National Semiconductor LM2733Y (PWM)
Voltage multiplier mechanism	7-stage charge pump (0603 1.0μF caps)	7-stage charge pump (0402 0.1μF caps)	1:9 turns ratio custom transformer (Taiyo Yuden NR3012 core)

Fig. 10. Efficiency vs. output power for hybrid and autotransformer voltage converters at 150V and 200V output.

back down to zero [26]. Regulation of the output voltage is achieved by varying the switching frequency.

4) Experimental Realization

Several implementations of the hybrid voltage multiplier and autotransformer boost converter have been tested. The relevant details are listed in Table V. The regulators were selected to best match the output power capabilities of each design. Pulse frequency modulation (PFM) regulators tend to be more efficient at low output power, making them a better match for the capacitive charge pumps in the hybrid converters, while pulse width modulation (PWM) regulators were used for the more powerful autotransformer converter. All components are off-the-shelf except for the autotransformer, which was fabricated using the Taiyo Yuden NR3012 30mg inductor core. Using a smaller core, such as the TDK VLF3012 series, which weighs around 10mg with shielding removed, can further reduce the weight of this design.

The components of the three designs weigh from 80mg to 150mg, not including the circuit board, and occupy from 0.5cm^2 to 1.5cm^2 of double-sided circuit board space, making them suitable for integration into the 0.5g and 1g MAV configurations described in Section III. Since packaging can account for as much as 90% of integrated circuit weight, it is possible to reduce the weight of the power electronics further by using bare-die versions of the components. This improvement will not, however, translate to inductive and capacitive components, which have low packaging overhead.

The measured efficiency vs. output power for the three designs at 150V and 200V output is shown in Fig. 10. Hybrid converters achieve higher efficiency at low output power, while the autotransformer converter leverages its lower component count and higher output current to provide a higher power density. It should also be noted that the autotransformer converter has better output voltage regulation (less than 1% variation, vs. 5% for the hybrid converters). Beyond the weight budget, the choice of topology should therefore be governed by the output power and voltage regulation requirements.

Efficiency numbers are in agreement with previous results for hybrid converters [3], and about 10-15% lower than previous results for autotransformer boost converters for
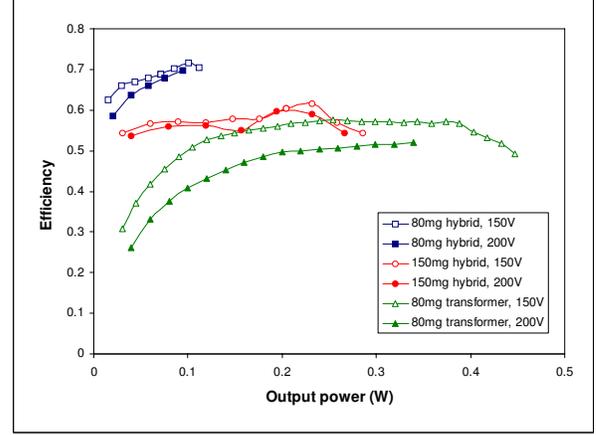
a comparable output power range [24]. This reduction is attributed to increased losses in the transformer due to miniaturization, and can be mitigated through better core design and winding technique.

Efforts are underway to realize a PT-based voltage converter. Radial mode PTs [25] 3-5mm in diameter and weighing 10-50mg have been fabricated. As of the time of this writing, the voltage gain of the fabricated PTs (under 10) is insufficient for the target application. Future work will focus on attempting to boost the voltage gain by using high-Q piezoelectric materials and varying PT geometry.

5) Driving Stage

Due to significant losses associated with using analog amplifiers for high-voltage driving, switching electronics are generally preferred [27]. A simple push-pull driver, such as the one described in [3], can produce a unipolar square wave voltage across the load. High-voltage MOSFETs and bipolar transistors are available in SOT-363 and SOT-23 packages in dual configurations, suggesting that a two-channel driver could be implemented using components weighing as little as 20mg, not including the board.

The capacitive nature of voltage-mode actuators allows for this drive scheme to be combined with a charge recovery circuit, as in [27], in order to boost actuator efficiency. This requires additional switches and inductive components. Assuming only the energy stored in the primary capacitance of the actuator will be recovered, as opposed to the energy stored in all higher resonant modes, only a small inductance would be necessary.

VI. SUMMARY AND FUTURE WORK

Using the models and estimates obtained for the mechanical and aerodynamic components, the actuation mechanism, the power electronics, and the battery, allows one to calculate the achievable flight time according to Eq. 1. Table VI summarizes the actuation mechanisms and power electronics

TABLE VI

ESTIMATED SYSTEM PERFORMANCE OF MAV CONFIGURATIONS

Mass (g)	Flapping frequency (Hz)	Max. battery capacity (mAh): discrete [bare die]	Max. flight time (minutes): discrete [bare die]
Piezoelectric bimorph cantilever			
Power electronics: hybrid, autotransformer, or piezo transformer with switching transistor driving stage and charge recovery.			
0.1	40	n/a [0.32]	n/a [3.61]
0.1	80	n/a [0.27]	n/a [2.10]
0.1	100	n/a [0.22]	n/a [1.64]
0.1	200	n/a [0.12]	n/a [0.62]
0.5	40	3.52 [6.02]	5.44 [9.30]
0.5	80	4.47 [6.81]	4.89 [7.45]
0.5	100	4.16 [6.65]	4.07 [6.52]
1.0	40	10.0 [12.3]	6.57 [8.00]
1.0	80	11.1 [13.0]	5.12 [5.98]
SMA bending cantilever			
Power electronics: buck or boost regulator with switching transistor driving stage.			
0.5	40	1.92 [3.00]	0.56 [0.88]
Dielectric elastomer linear extender			
Power electronics: hybrid, piezo transformer.			
n/a - weight of power electronics exceeded all MAV weight budgets			

configurations capable of driving one or more MAV configurations. Both discrete and bare-die versions of the electronic components are considered. Based on previous work on sub-10mg flight control sensors [28] and lightweight, low-power controllers [29], 10% of the weight budget is allotted to sensors and control electronics. Where the weight budget of the MAV exceeds the weight of its mechanical, actuating, sensing, and electronic components, a battery capacity is estimated based on remaining weight budget and used to determine the robot flight time, with the three longest flight times highlighted in the table. Piezoelectric, dielectric elastomer, and (for smaller sizes and low flapping frequencies) shape memory actuators are capable of powering the MAVs.

Calculations show that the power circuits presented in this paper become too heavy when configured to generate the kV-range voltages necessary to excite dielectric elastomer actuators. SMA-powered robots enjoy lighter, more efficient power electronics, but flight time is reduced severely by the low efficiency of the actuator. Piezoelectric actuators are expected to be widely applicable to flapping-wing MAVs in the weight ranges considered in this paper, enabling longer flight times. The Harvard Microrobotic Fly, which has achieved liftoff, serves as a proof of concept device for piezoelectric flying robots.

Future work will involve the continued improvement of the power circuits presented in this paper and integration of the power electronics package into an appropriately sized MAV platform.

REFERENCES

[1] S. Avadhanula, "Design, fabrication, and control of the micromechanical flying insect," Ph.D. dissertation, U. C. Berkeley, 2006.
[2] R. J. Wood, "Liftoff of a 60mg flapping-wing MAV," in *IEEE/RSJ Int. Conf. on Intelligent Robots and Systems*, 2007, pp. 1889–1894.
[3] E. Steltz, M. Seeman, S. Avadhanula, and R. S. Fearing, "Power electronics design choice for piezoelectric microrobots," in *IEEE/RSJ Int. Conf. on Intelligent Robots and Systems*, 2006, pp. 1322–1328.
[4] H. Y. Chan, J. H. M. Lam, and W. J. Li, "A biomimetic flying silicon microchip: Feasibility study," in *IEEE Int. Conf. on Robotics and Biomimetics*, 2004, pp. 447–451.
[5] S. Sane and M. Dickinson, "The aerodynamic effects of wing rotation and a revised quasi-steady model of flapping flight," *J. of Experimental Biology*, vol. 205, no. 8, pp. 1087–1096, April 2002.
[6] C. Ellington, "The aerodynamics of hovering insect flight II: Morphological parameters," *Phil. Trans. R. Soc. B*, vol. 305, no. 1122, pp. 17–40, 1984.
[7] C. Ellington, "The novel aerodynamics of insect flight: Applications to micro-air vehicles," *J. of Experimental Biology*, vol. 202, no. 23, pp. 3439–3448, December 1999.
[8] R. Dudley, *The Biomechanics of Insect Flight: Form, Function and Evolution*. Princeton University Press, 1999.
[9] W. C. Tang, T. C. H. Nguyen, and R. T. Howe, "Laterally driven polysilicon resonant microstructures," in *Proc. Micro Electro Mechanical Systems*, 1989, pp. 53–59.
[10] Q. M. Wang and L. E. Cross, "Performance analysis of piezoelectric cantilever bending actuators," *Ferroelectrics*, vol. 215, no. 1-4, pp. 187–213, 1998.
[11] S. Prasanna and S. M. Spearing, "Materials selection and design of microelectrothermal bimaterial actuators," *J. of Microelectromechanical Systems*, vol. 16, no. 2, pp. 248–259, April 2007.
[12] P. Krulevitch, *et al.*, "Thin film shape memory alloy microactuators," *J. of Microelectromechanical Systems*, vol. 5, no. 4, pp. 270–282, 1996.
[13] R. D. Kornbluh, *et al.*, "Electroelastomers: Applications of dielectric elastomer transducers for actuation, generation, and smart structures," in *Proc. SPIE*, vol. 4698, 2002, pp. 254–270.
[14] P. B. Chu, P. R. Nelson, M. L. Tachiki, and K. S. J. Pister, "Dynamics of polysilicon parallel-plate electrostatic actuators," *Sensors and Actuators A*, vol. 52, no. 1-3, pp. 216–220, March 1996.
[15] H. S. Carslaw and J. C. Jaeger, *Conduction of Heat in Solids*. Oxford University Press, 1986.
[16] D. R. Madill and D. Wang, "Modeling and L2-stability of a shape memory alloy position control system," *IEEE Trans. on Control Systems Technology*, vol. 6, no. 4, pp. 473–481, July 1998.
[17] S. Hollar, A. Flynn, C. Bellew, and K. S. J. Pister, "Solar powered 10 mg silicon robot," in *Proc. IEEE Sixteenth Annual Int. Conf. on Micro Electro Mechanical Systems*, 2003, pp. 706–711.
[18] J. D. Madden and L. Filipozzi, "Web-based actuator selection tool," *Proc. SPIE*, vol. 5759, pp. 9–15, 2005.
[19] J. H. Marden, "Variability in the size, composition, and function of insect flight muscles," *Annu. Rev. Physiol.*, vol. 62, pp. 157–78, 2000.
[20] A. Schneuwly, "Charge ahead (ultracapacitor technology and applications)," *Power Engineer*, vol. 19, pp. 34–37, February 2005.
[21] A. Wilhelm, B. W. Surgenor, and J. G. Pharoah, "Evaluation of a micro fuel cell as applied to a mobile robot," in *IEEE Int. Conf. on Mechatronics and Automation*, 2005, pp. 32–36.
[22] C. L. Bellew, S. Hollar, and K. S. J. Pister, "An SOI process for fabrication of solar cells, transistors and electrostatic actuators," in *IEEE Int. Solid-State Sensors and Actuators Conf.*, June 2003, pp. 1075–1078.
[23] J. F. Saheb, J. F. Richard, M. Sawan, R. Meingan, and Y. Savaria, "System integration of high voltage electrostatic MEMS actuators," *Analog Integrated Circuits and Signal Processing*, vol. 53, pp. 27–34, October 2007.
[24] "Small, high-voltage boost converters," Maxim Semiconductor Application Note 1109, 2002.
[25] K. Uchino, B. Koc, P. Laoratanakul, and A. V. Carazo, "Piezoelectric transformers: New perspective," *Ferroelectrics*, vol. 263, no. 1-4, pp. 91–100, 2001.
[26] E. Dallago, A. Danioni, G. Ricotti, and G. Venchi, "Single chip, low supply voltage piezoelectric transformer controller," in *Proc. of the 29th European Solid-State Circuits Conf.*, September 2003, pp. 273–276.
[27] D. Campolo, M. Sitti, and R. S. Fearing, "Efficient charge recovery method for driving piezoelectric actuators with quasi-square waves," *Ultrasonics*, vol. 50, no. 3, pp. 237–244, March 2003.
[28] W. C. Wu, L. Schenato, R. J. Wood, and R. S. Fearing, "Biomimetic sensor suite for flight control of a micromechanical flying insect: design and experimental results," in *IEEE International Conference on Robotics and Automation*, vol. 1, 2003, pp. 1146–1151.
[29] B. A. Warneke and K. S. J. Pister, "An ultra-low energy microcontroller for Smart Dust wireless sensor networks," in *IEEE Int. Solid-State Circuits Conf. 2004*, vol. 1, 2004, pp. 316–317.